



# Comparison of Cu–Al–Ni–Mn–Zr shape memory alloy prepared by selective laser melting and conventional powder metallurgy

Dennis GERA<sup>1,2</sup>, Jonadabe SANTOS<sup>1,2</sup>, Cláudio S. KIMINAMI<sup>1,2</sup>, Piter GARGARELLA<sup>1,2</sup>

1. Postgraduate Program in Materials Science and Engineering, Federal University of São Carlos, São Carlos, Brazil;

2. Materials Engineering Department, Federal University of São Carlos,

R. Washington Luís, km 235-SP 310, São Carlos, Brazil

Received 22 February 2020; accepted 20 September 2020

**Abstract:** This work aimed to investigate and critically analyze the differences in microstructural features and thermal stability of Cu–11.3Al–3.2Ni–3.0Mn–0.5Zr shape memory alloy processed by selective laser melting (SLM) and conventional powder metallurgy. PM specimens were produced by sintering 106–180  $\mu\text{m}$  pre-alloyed powders under an argon atmosphere at 1060 °C without secondary operations. SLM specimens were consolidated through melting 32–106  $\mu\text{m}$  pre-alloyed powders on a Cu–10Sn substrate. Mechanical properties were measured through Vickers hardness testing. Differential scanning calorimetry was conducted to assess the martensitic transformation temperatures. X-ray diffraction patterns were collected to identify the metallurgical phases. Optical and scanning electron microscopy was used to analyze the microstructural features.  $\beta'_1$  martensite was found, irrespective of the processing route, although coarser martensitic variants were present in PM-specimens. In conventional powder metallurgy samples, intergranular eutectoid constituents and stabilized austenite also formed at room temperature. PM-specimens showed similar average hardness values to the SLM-specimens, albeit with high standard deviation linked to the porosity. The specimens processed by SLM showed reversible martensitic transformation ( $T_0=171$  °C). PM-processed specimens did not show shape memory effects.

**Key words:** shape memory alloys; powder metallurgy; additive manufacturing; selective laser melting; Cu-based alloys

## 1 Introduction

Arne ÖLANDER first discovered shape memory alloy (SMA) in 1932, but the importance of shape-memory materials was only recognized when William BUEHLER and Frederick WANG revealed the shape memory effect of nickel–titanium (NiTi) alloys in 1962 [1,2]. Since then, SMAs have been at the forefront of research, being used for a wide variety of applications in various fields, such as structural, industrial, automotive, aerospace, and biomedical [3–6]. Due to biocompatibility, good mechanical properties, and shape memory effect (SME), NiTi-based SMAs

have long been preferable for most applications [7]. However, NiTi alloys' high cost, combined with the market's search for properties that attend to specific requirements, has sky-rocketed the scientific development of Cu-based SMAs, such as the Cu–Al–Ni system [8–10]. Cu-based SMAs provide good electrical resistivity ( $\rho=2.8\times 10^{-4}$   $\Omega\cdot\text{mm}$  [11]) and thermal conductivity ( $k=83$  W/(m·K) [12]) compared to NiTi alloys ( $\rho=8.3\times 10^{-4}$   $\Omega\cdot\text{mm}$  [13] and  $k=28$  W/(m·K) [13]). Besides, lower cost and easier processing of Cu-based alloys make them attractive alternatives. However, due to the high anisotropy of Cu-based alloys and, in some cases, the coarse grains [14], the Cu–Al–Ni system generally presents poor mechanical properties with

an intergranular fracture [15], making it necessary to use alloying elements to improve said properties. Nonetheless, it is known that the transformation temperatures of Cu-based SMA are highly dependent on composition [16–19] and that different processing routes can lead to different mechanical properties [20,21].

A powder-based processing route that has become an increasing trend in industries and scientific studies is additive manufacturing (AM), showing an annual growth rate of 26% in the last 20 years [22]. This technology began in the fields of photo sculpture and topography [23] and has extended today to various niches, such as rapid prototyping, production of spare parts, customized items, and small batches. Through layer-by-layer production, AM has made possible manufacture of any product no matter the complexity, allowing for interconnected pores, overlapping grids, and other specific requirements. One of the most widely used AM techniques in metals is selective laser melting (SLM), which consists of melting predetermined sites, layer-by-layer of powder, to create the product designed in a 3D CAD software. Although it has been reported that the processability of pure copper using SLM is limited due to its high reflectivity and conductivity [24], various works have proven that it is possible to obtain Cu-based SMAs with good SME and thermal stability, as well as fine grains that reduce the effect of Cu anisotropy [25–27], hence enhancing mechanical properties.

However, SLM is mostly criticized for its low productivity, requiring much time to manufacture products [28]. This has led to the development of new technologies that aim to increase productivity without jeopardizing the advantages of layer-by-layer manufacturing. In some cases, however, these technologies are more similar to powder metallurgy (PM) than to additive manufacturing, incurring significant differences in the overall properties of the product. Desktop Metal, for example, has developed a 3D metal printing system, Studio System™, which claims to be the most affordable and simplest 3D printer [29] in the market. Studio System™ works by extruding bound metal rods (metal powder held together by wax and polymer binder) layer-by-layer, creating the desired green product. This product is then debinded and sintered, as produced by powder metallurgy. This

process subjects the specimen to a significant amount of time under high temperatures when compared to additive manufacturing. Therefore, one cannot expect the microstructural features and mechanical properties of a product manufactured by SLM and by the Studio System™ process to be the same.

PM presents many challenges, such as high porosity, density gradient, and, in some cases, the need for secondary operations. Successful attempts to manufacture Cu-based SMAs have already been reported in the literature. TANG et al [30] processed Cu–14Al–4Ni by conventional powder metallurgy using extended milling and sintering but had to subject the samples to a solution treatment at 900 °C for 1 h to achieve better material properties. In summary, both powder metallurgy and additive manufacturing exhibit different advantages and disadvantages when it comes to processing Cu-based SMAs. This work aims to assess a comparative analysis in which the microstructural features and thermal stability of the Cu–11.3Al–3.2Ni–3.0Mn–0.5Zr alloy are studied and correlated to the processing conditions of conventional PM and SLM.

## 2 Experimental

Pre-alloyed powders were obtained by gas atomization of a master ingot with composition of Cu–11.8Al–3.2Ni–3Mn–0.5Zr. The preparation of the ingot was conducted with a vacuum induction furnace VIM–Inductotherm 50-30 R using high purity elements (>99.5%). Atomization was carried out with a HERMIGA atomizer from Phoenix Scientific Industries using pressure of 8.0 MPa, 3 mm diameter nozzle, and superheating of 150 °C. The solidified powders were sieved into different size ranges. The range used for specimens produced by powder metallurgy was 106–180 μm, and the specimens manufactured by SLM were prepared using powder with granulometry ranging 32–106 μm.

In powder metallurgy, the pre-alloyed powder was pressed into a cylindrical shape using a steel tool die with the dimensions of 5 mm in diameter and approximately 10 mm in height. The compaction was conducted with oleic acid as a lubricant with an applied maximum pressure of

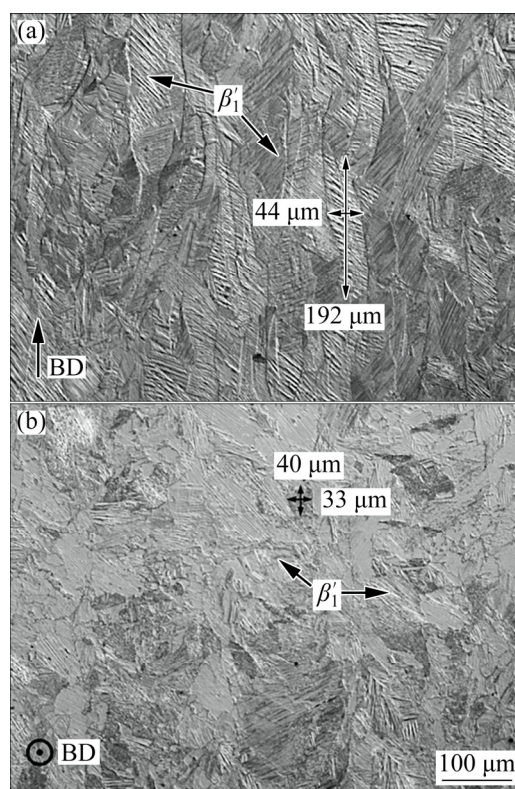
1300 MPa. Sintering parameters were established in a preliminary optimization work [31] and, therefore, sintering was carried out under an argon atmosphere at 1060 °C for 1.5 h with a heating rate of 10 °C/min. The specimens were cooled down at relatively slow rates provided by air cooling. Sintering was conducted using a furnace model CPU-10P-LCD from EDG. Selective laser melting was carried out at the Leibniz Institute for Solid State and Materials Research, Dresden, Germany. The equipment used was the SLM 250 HL, manufactured by SLM Solutions GmbH, which uses an Nd-YAG crystal for obtaining a continuous laser beam with a maximum power of 400 W. The beam diameter and layer thickness used were 80 and 110  $\mu\text{m}$ , respectively. Specimens were produced using a Cu–10Sn substrate and a unidirectional scanning with 90° rotation. The parameters used for processing were based on preliminary work for process optimization [32], in which power ( $P$ ), scanning velocity ( $V$ ), and hatching percentage ( $S$ ) were studied. In this work, the optimized combination of parameters was used, that is,  $P=330$  W,  $V=740$  mm/s, and  $S=40\%$ .

Differential scanning calorimetry (DSC) was conducted with the sintered and additive-manufactured specimens to measure the martensitic phase transformation temperatures. For DSC measurements, a Netzsch 200F3 was used to analyze a low-temperature range (50–250 °C). In all cases, a heating rate of 10 K/min was applied. For the microstructural investigation, the specimens were ground by sandpaper and polished with 1  $\mu\text{m}$  grade alumina suspension. The etching was carried out using a solution of  $\text{FeCl}_3$ , HCl and  $\text{H}_2\text{O}$  for 8 s. The microstructures were observed using a light optical microscopy (Olympus BX41M-LED) and a scanning electron microscopy (SEM) (Phillips XL30). Grain size measurements were conducted with the linear intercept method using the software ImageJ. In this case, at least three images were examined for each condition. X-ray diffraction patterns were collected using a Bruker D8 Advance within the  $2\theta$  range of 20°–90° and a step of 2 (°)/min. Density measurements were carried out by the Archimedes principle. Hardness was measured in cylindrical specimens of 3 mm (SLM) and 5 mm (PM) using a load of 200 g for a holding time of 15 s in a Shimadzu Vickers hardness tester.

## 3 Results and discussion

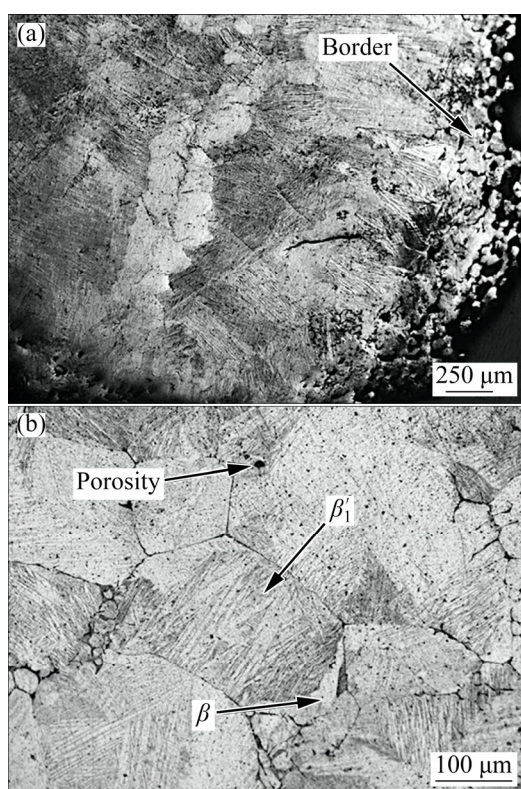
### 3.1 Microstructure and phase formation

Figure 1 shows the micrographs from the samples manufactured by SLM. Figure 1(a) corresponds to the longitudinal cross-section and depicts elongated grains with an average width and length of  $(45\pm 5)$   $\mu\text{m}$  and  $(190\pm 17)$   $\mu\text{m}$ , respectively. The elongated grain morphology is formed in the maximum heat flow direction (normal to the solidification front), and therefore, is not seen in the transverse cross-section (Fig. 1(b)), which shows grains with an average size of  $(35\pm 4)$   $\mu\text{m}$ . Directional growth is an intrinsic microstructural characteristic of additive manufacturing due to the layer-by-layer processing, and, although there are techniques to avoid such feature, none was used in this work. From Fig. 1, it becomes clear that only  $\beta'_1$  phase, characterized by a zig-zag morphology, was formed upon rapid cooling. Furthermore, the specimens produced with the optimal combination of parameters presented a density of 97% relative to the theoretical density (8.19 g/cm<sup>3</sup>), accompanied by very low porosity.



**Fig. 1** Optical microscopy images of longitudinal (a) and transverse (b) section of Cu–11.3Al–3.2Ni–3Mn–0.5Zr alloy produced by SLM (BD–Building direction)

From the micrograph of the sample processed by PM (Fig. 2), it is possible to identify significant differences in the microstructural characteristics in comparison to the material processed by SLM. Conventional powder metallurgy produced very porous samples, with a maximum relative density of 88%. This was expected due to low green relative density, 76%, presented in the samples before sintering as a consequence of uniaxial compaction, leading to various pores in the grain boundaries, where the material necking and densification occurred. Moreover, it is possible to notice the presence of irregular pores concentrated near the border of the specimen, as indicated in Fig. 2(a). This is due to the nature of uniaxial pressing, which creates a density gradient in the compacted green specimen.



**Fig. 2** Optical microscopy images of Cu-11.3Al-3.2Ni-3Mn-0.5Zr alloy produced by powder metallurgy

It is important to reiterate that under the studied conditions of conventional powder metallurgy, it was not possible to achieve a more relatively dense specimen, nor a more refined microstructure in processing Cu-11.3Al-3.2Ni-3Mn-0.5Zr alloy. Higher sintering temperatures would lead to the melting of the alloy, and less

sintering time did not provide sufficient energy for the final sintering stages to occur correctly. Hence, it is the authors' understanding that SLM processing is more efficient in producing more dense specimens with fewer microstructural defects, despite the formation of anisotropic grains elongated in the direction of heat extraction.

Due to long time at elevated temperatures, the PM samples were given sufficient energy for grain growth, achieving an average size of  $(120 \pm 15) \mu\text{m}$ . Although the obtained grain size is significantly smaller than that reported in literature for alloys produced without Mn and Zr (1–3 mm) [16,18], SLM samples demonstrated grains smaller than PM samples. However, it is essential to reiterate that the specimens produced by PM were originated from a coarser granulometric powder, therefore influencing the final grain size. Figure 2(b) shows that the microstructure presents a zig-zag morphology, characteristic of  $\beta'_1$  martensite. However, Fig. 3 shows that the martensitic variants and spacing of the PM specimens are much larger than those found in SLM. This can be explained by the more extended time at high temperature, in which the martensitic variants were given enough energy to allow atom mobility. This behavior has also been reported by CAVA [21], in which a similar alloy was processed by spray forming and then heat-treated at 850 °C for different periods. It was found that heat treatment at more prolonged periods at this temperature led to an increase in grain size, formation of precipitates, and martensitic variants, as well as a decrease in hardness.

Nevertheless,  $\beta'_1$  martensitic structure was found despite the relatively slow cooling rate after sintering (air cooling), showing powder metallurgy to be reasonably consistent in developing a martensitic structure without severe quenching, as seen in Fig. 2(b). However, through optical microscopy, it is also possible to observe grains without a zig-zag morphology, suggesting that the austenitic  $\beta$  phase could still be present at room temperature. Retained austenite could be a consequence of element segregation during processing that, in turn, increased the stability of  $\beta$  phase. This hypothesis is further discussed with XRD and DSC analysis.

Higher magnifications of the obtained microstructure were used for a more in-depth

analysis of the martensitic variants and phases present. Figures 3(a) and 4 depict a scanning electronic micrograph and an X-ray diffraction pattern, respectively, of specimens processed by SLM. The XRD shows that only  $\beta'_1$  martensite was found in the SLM specimen, which is in agreement with other reports of alloys with similar compositions [26,33]. Since Cu–Al–Ni alloys are generally quite resistant towards aging, it is suggested that the cooling rate was sufficiently large to avoid the formation of NiAl and the eutectoid  $\alpha$  (copper-rich solid solution)+ $\gamma_2$  (CuAl) structure, despite the detection limit of XRD (>5 vol.%) not permitting a complete analysis. Therefore, it is likely that the microstructure presented in Fig. 3(a) exclusively demonstrates  $\beta'_1$  martensite.

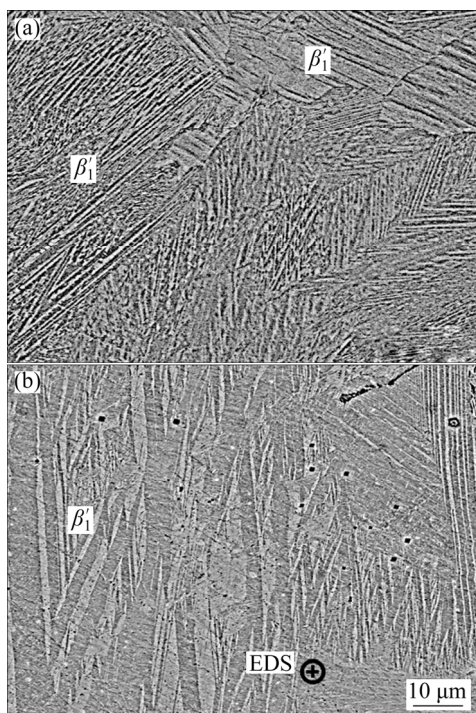


**Fig. 3** Scanning electronic micrographs of Cu–11.3Al–3.2Ni–3Mn–0.5Zr alloy processed by selective laser melting (a) and powder metallurgy (b) with EDS spot indication

Nevertheless, GUSTMANN et al [20] processed a similar alloy through SLM and used transmission electron microscopy (TEM) and EBSD for complementary measurements. While the matrix was also identified as  $\beta'_1$  martensite, the second phase  $\text{Cu}_2\text{ZrAl}$  nanoparticles,  $Y$  phase, were found finely dispersed inside the grains. It was discussed that since the location of these particles is

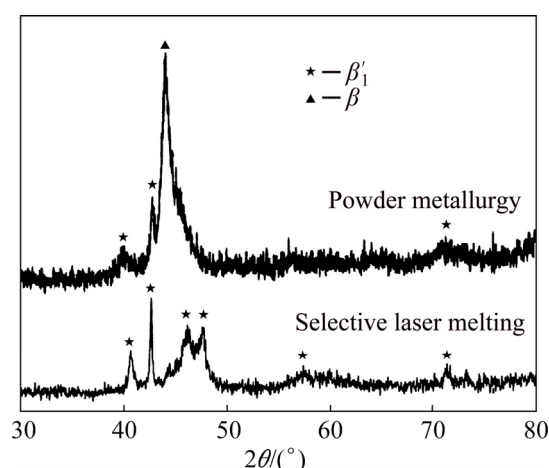


**Fig. 4** X-ray diffraction pattern of Cu–11.35Al–3.2Ni–3Mn–0.5Zr processed by SLM and PM

not particularly at the grain boundaries, then it cannot be responsible for impeding grain growth. Instead, it is the dissolved Zr that slows down such growth. However, they also found that a subsequent annealing treatment coarsens the  $Y$  phase, which then segregates to the boundaries and impedes coarsening. Therefore, in SLM specimens, since the material is rapidly melted and cooled and does not undergo annealing treatment, the secondary  $Y$  phase is not encountered as an intergranular phase.

The scanning electronic micrograph of the specimen processed by powder metallurgy (Fig. 5) contains severe discrepancies in comparison to the one manufactured by SLM. Initially, it is possible to notice the zig-zag martensitic morphology already discussed in Fig. 2. Also, higher magnifications detected an interdendritic structure with lamellar morphology, suggesting a eutectoid constituent. This phase most likely was originated from the formation of a liquid phase during sintering. GERA et al [31,34] reported that it was necessary to use a sintering temperature near the melting point of the alloy to obtain good sintering properties, although it is reported in the literature that the ideal sintering temperature is between  $0.6T_m$  and  $0.8T_m$  [35]. This suggests that the Cu–11.35Al–3.2Ni–3Mn–0.5Zr alloy cannot be processed by conventional powder metallurgy without the aid of liquid sintering. As a consequence, the relatively slow cooling rate imposed on the liquid probably provided enough time and energy for the equilibrium decomposition of  $\beta$  (austenite)  $\rightarrow \alpha + \gamma_2$  or  $\beta \rightarrow \alpha + \text{NiAl}$  to occur at the grain boundaries.

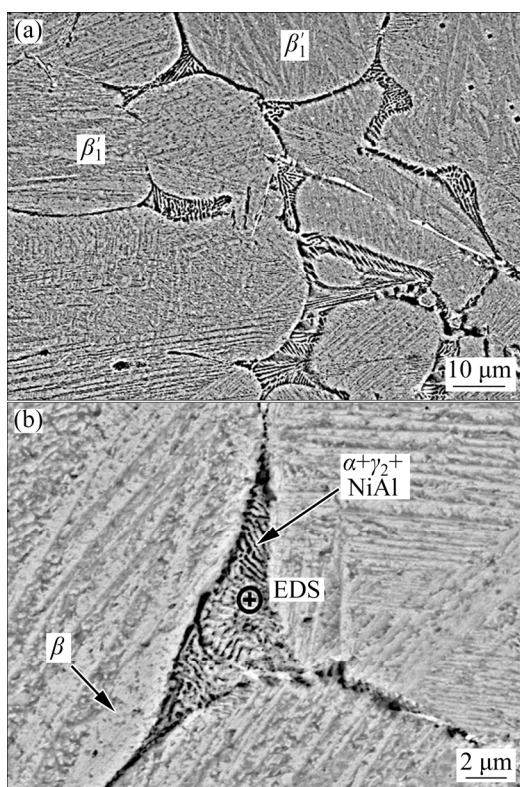


**Fig. 5** Scanning electronic micrographs of Cu-11.3Al-3.2Ni-3Mn-0.5Zr alloy processed by powder metallurgy with EDS spot indication

The XRD analysis of the PM-specimen is contained in Fig. 4. Besides  $\beta'_1$  martensite, the presence of  $\beta$  was also found. This is explained due to the specimen being subjected to high temperatures under an extended period, which led to atom diffusion and austenitic stabilization. GERA et al [34] have reported this behavior by conducting a study in which sintering time was varied and analyzed the differences in phase formation through XRD analysis. It was found that the diffraction pattern exhibits  $\beta'_1$  martensite predominantly at shorter sintering time (i.e., 0.5 h), but as sintering time increases, these martensitic peaks start to diminish and the peak referring to  $\beta$  becomes intenser and more stable. Due to a prolonged sintering time, which was necessary to obtain good relative density, the material was given enough heat input for high atom diffusion, causing element segregation and enhancing  $\beta$  stability. Hence, powder metallurgy showed to be consistent in forming martensite when shorter sintering time and air-cooling are applied, but as the need for a denser specimen is required, and therefore longer

sintering time is needed, austenite stability is enhanced. Such behavior explains the intensity of the austenite peak in Fig. 4, which is substantially high compared to that of the martensite phase, indicating that the PM specimen has a higher content of austenite than martensite, compromising the SME.

The X-ray diffraction pattern showed no evidence of  $\alpha$  or  $\gamma_2$  or NiAl, although, according to BREZINA [36], it is not possible to distinguish between  $\gamma_2$  and NiAl by optical microscopy nor by XRD since the lattice parameter of  $\gamma_2$  is three times that of NiAl so that many peaks of the X-ray diffraction patterns of  $\gamma_2$  and NiAl are superimposed. However, by analyzing the SEM image in Fig. 5(b) and the corresponding equilibrium phase diagram, it is possible to conclude that the lamellar structure found in between the grain boundaries is formed by the eutectoid transformation of  $\beta \rightarrow \alpha + \gamma_2 + \text{NiAl}$ . Therefore, the absence of peaks corresponding to these phases could be explained by the small contents outside the detection limit of XRD, since the volume of the eutectoid structure is much smaller relative to the average grain boundary size.

Since the specimen produced by powder metallurgy was not analyzed by transmission electron microscopy, it is not possible to confirm the presence of the finely dispersed second phase  $Y$ . However, as discussed by GUSTMANN et al [20], it was seen that a supersaturated matrix could precipitate and segregate large  $Y$  phase particles to the boundaries when cooled at slower rates and annealed, respectively. Since the specimen produced by PM was air-cooled and maintained at high temperatures for a relatively long period, the formation and segregation of the  $Y$  phase are suspected.

An energy-dispersive X-ray spectroscopy analysis was used to identify the compositional elements of specific sites. Table 1 depicts the average EDS analysis results of the matrix and the intergranular constituent from eight measurements. Even though similar compositions were found in both locations, the intergranular constituent is distinguished by a higher zirconium content, which is possibly correlated to the segregation of  $Y$  phase. Furthermore, apart from Zr, all other elements were found in similar contents in the matrix and the intergranular constituent.

**Table 1** Energy-dispersive X-ray spectroscopy analysis results of matrix and intergranular constituent (wt.%)

Element	Matrix	Intergranular constituent
Cu	80.69	81.02
Al	13.78	13.39
Mg	3.21	3.03
Ni	1.36	1.24
Zr	0.98	1.34

The microstructural analysis of the specimens processed by SLM and PM confirms that additive manufacturing is more efficient in producing a specimen with fine  $\beta'_1$  martensitic microstructure and high relative density. Also, the rapid cooling rates in SLM processing lead to finely dispersed nanoparticles that are not given enough time nor energy for segregation towards the grain boundaries. In contrast, the specimens produced by PM presented 9% higher porosity, significant defects, and intergranular phases that may compromise mechanical properties.

### 3.2 Mechanical properties

The average microhardness values obtained from the SLM specimens, HV ( $260 \pm 7$ ), were found to be higher than those encountered in the specimens processed by PM, HV ( $244 \pm 60$ ). Although there is only a slight difference, this can be attributed to the finer grains and the residual stresses generated during SLM processing. Moreover, the presence of finely dispersed  $\text{Cu}_2\text{ZrAl}$  phase inside the grains from SLM-fabricated specimens and the finer martensite spacing may also be responsible for increased strength of the material. As mentioned earlier, although the specimen processed by PM also contains Zr and is, therefore, susceptible to the formation of  $\gamma$ -phase, the increased heat exposure most likely led to the diffusion of  $\text{Cu}_2\text{ZrAl}$  to the grain boundaries, lowering the grains capability to impede dislocation movement. It is also noteworthy to mention that the hardness tests conducted in the SLM specimen were carried out in the center and near the sample's surface with no significant differences between the values for these regions. This shows that SLM was capable of processing these small-diameter samples with similar properties throughout the cross-section of the specimen. The same observation was not

found in the samples produced by PM. Due to the nature of uniaxial compression, some regions suffer higher levels of pressure than others, leading to a density gradient. The compacted material shows a higher density in regions near the compaction piston and the center. The material localized near the die wall, however, presents significant lower levels of porosity. As a result, the PM-processed specimen has a much larger standard deviation in microhardness when compared to SLM, since there are porous and dense regions influencing the measurement.

### 3.3 Thermal stability

Differential scanning calorimetry (DSC) analysis was used to obtain the transformation temperatures of the samples processed by SLM and PM. Figure 6 shows the heating and cooling curves of the specimens manufactured by selective laser melting and powder metallurgy with the corresponding optimized processing parameters.

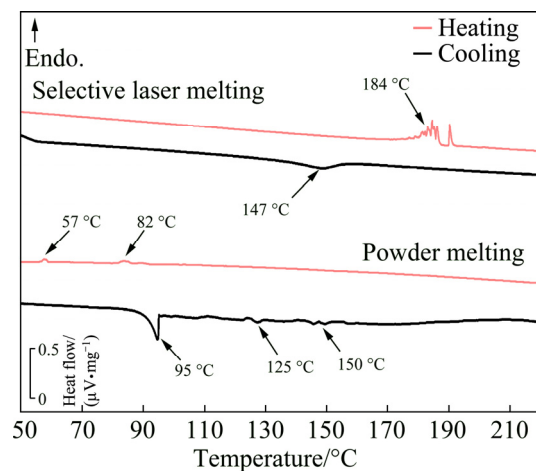


**Fig. 6** DSC curves of specimens processed by SLM and PM with optimized parameters

The DSC curves indicate many differences between the specimens. On the SLM curve, the endothermic peaks (positive heat flow) in the thermogram correspond to the reverse transformation (martensite  $\rightarrow \beta$ ) at 184 °C and the exothermic peaks (negative heat flow) are linked to the forward transformation ( $\beta \rightarrow$  martensite) at 147 °C. Upon heating, peaks of jerky nature appear at 184 °C. This behavior has already been reported in other studies of Cu-based SMAs and has been linked to the  $\gamma'_1 \rightarrow \beta$  transformation [16,17].

However, scanning electron microscopic images and X-ray diffraction analysis have confirmed that only  $\beta'_1$  martensite is present in the microstructure; therefore, these peaks cannot be linked to  $\gamma'_1$ . GUSTMANN et al [20] propose that the jerky reverse transformation is due to the presence of a finely-dispersed  $Y$  phase, which pins the moving interfaces during the martensitic transformation and causes spikes in thermal analysis. Moreover, the obtained transformation temperatures are relatively high although studies have shown that increasing the contents of Al and Ni [17], and adding alloying elements, such as Mn, Zr and Ti [10,16,18], can decrease the transformation temperatures of the alloy.

The results obtained from the thermal analysis of the specimen fabricated by PM are significantly different. During heating, two peaks are found at 57 and 82 °C. They may refer to a two-stage martensitic transformation,  $\beta'_1 \rightarrow \beta$  and  $\gamma'_1 \rightarrow \beta$  [37], and this is highly unlikely due to the absence of  $\gamma'_1$  in the XRD analysis and to the small area of these peaks. Austenitic transformations are generally characterized by well-defined peaks in a DSC analysis [16,17]. Besides, it was expected that austenite would occur at a higher temperature since it has already been reported in the literature that transformation temperatures are independent of porosity [38] and that coarser grains lead to higher martensitic and austenitic temperatures due to the poor  $\beta$  stabilization [39,40]. Therefore, it is most likely that the phenomena occurring at 57 and 82 °C are not related to austenitization; however, further experimentation, such as in-situ XRD, is required for confirmation.

The resulting curve of the PM specimen during cooling is also unusual. Several low-enthalpy peaks appear between 155 and 120 °C, followed by a well-defined exothermic peak at 95 °C. Typically, it would be suggested that the latter corresponds to a martensitic transformation temperature; however, as discussed earlier, no austenitic transformations occurred during heating; hence, it is highly unlikely that the 95 °C peak refers to a martensitic transformation. Due to the absence of a well-defined peak during heating and the presence of only one peak during cooling, it is suggested that, at 95 °C, phase ordering takes place, lowering the free energy of the system. As for abnormal behavior on the cooling curve between 155 and 120 °C,

further experimentation is required to identify the phenomena.

GERA [31] studied the influence of sintering time on the properties of PM-fabricated specimens and found that at shorter sintering time, the peaks that appear in DSC analysis during heating and cooling are less pronounced than those at longer sintering time. Besides, as discussed earlier, it was also found that sintering for more extended periods also increased the intensity of the  $\beta$  peak in XRD analysis. This suggests that the stabilization of austenite due to higher heat input and atom diffusion plays a significant role in the thermal behavior of the material.

The curves depicted in Fig. 7 exhibit the start and finish temperatures for forward and reverse transformations. It was found that the specimens processed by SLM present  $A_s$  and  $M_f$  temperatures of 172 and 132 °C, respectively; while the PM-processed specimen does not appear to undergo reverse nor forward transformations upon heating and cooling, despite the observation of martensitic grains in Figs. 2 and 4. Hence, it is observed that products manufactured by conventional powder metallurgy using the same processing parameters discussed in this work do not present a good shape memory effect and, therefore, such process has to be adjusted for industry use.

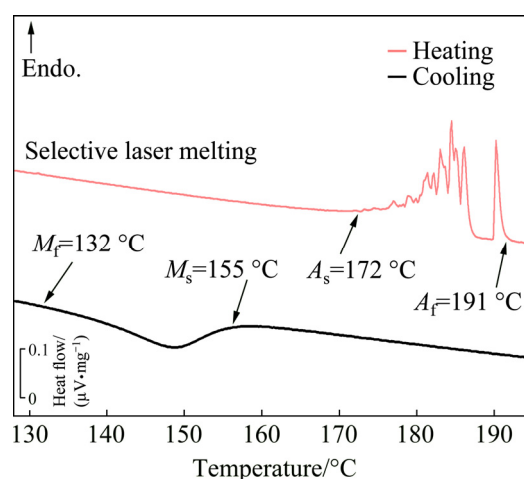


**Fig. 7** DSC curves of specimens processed by SLM, indicating start and finish temperatures for forward and reverse transformations

Furthermore, essential concerns among SMAs are the thermal hysteresis of the alloy,  $T_H$ , and equilibrium temperature,  $T_0$ , calculated by the following equations:

$$T_H = A_f - M_s; T_0 = 1/2(A_f + M_s) \quad (1)$$

Small hysteresis of shape memory alloy is attractive as the temperature window for actuation force, or displacement is small and facilitates a fast response [37]. The thermal hysteresis between the forward and reverse transformation of the SLM-processed specimen is 38 °C, which is, in most cases, relatively higher or similar to what is found in other SMAs [16,17]. Regarding the equilibrium temperature, the higher the  $T_0$  is, the more stable the martensitic phase is. In this case, the specimen produced by SLM shows significantly high equilibrium temperature (175 °C), meaning that products fabricated by SLM are well suited to maintain a martensitic structure in applications that require high thermal stability. Due to the lack of transformation temperatures of the PM-processed specimen, a comparison of  $T_H$  and  $T_0$  between processing routes could not be attained.

## 4 Conclusions

(1) Selective laser melting was successful in producing samples with  $\beta'_1$  martensitic matrix, essential to have a shape memory effect. Regarding powder metallurgy, despite the formation of  $\beta'_1$  martensite, the austenitic  $\beta$  phase and secondary phases, such as  $\alpha + \gamma_2 + \text{NiAl}$ , became stable at room temperature and were formed at the grain boundaries, respectively.

(2) Microhardness tests showed that the specimens manufactured by SLM exhibit superior mechanical properties than the samples processed by PM. This superiority is predominantly correlated to finer grain sizes, fewer porosity, and higher martensitic content.

(3) Thermal analysis showed that due to high cooling rates, the specimens processed by SLM show good thermal stability and hysteresis. In contrast, the samples produced by powder metallurgy did not exhibit a forward nor reverse transformation during the heating and cooling in DSC analysis.

## Acknowledgments

The authors would like to acknowledge the financial support of CAPES (Coordination for the Improvement of Higher Education Personnel–

Brazil) and FAPESP (São Paulo Research Foundation–Brazil) under Projects 2013/05987-8, 2016/00583-4, and 2017/27031-4.

## References

- [1] AHMED Y M Z, ISKANDER B A, IBRAHIM M, SHALABI M E H. Mechanical properties and porosity relationship of porous iron compacts [J]. Powder Metallurgy, 2009, 52: 72–79.
- [2] BUEHLER W J, GILFRICH J V, WILEY R C. Effect of low-temperature phase changes on the mechanical properties of alloys near composition TiNi [J]. Journal of Applied Physics, 1963, 34: 1475–1477.
- [3] STOECKEL D. Shape memory actuators for automotive applications [J]. Materials and Design, 1990, 11: 302–307.
- [4] SUN L, HUANG W M, DING Z, ZHAO Y, WANG C C, PURNAWALI H. Stimulus-responsive shape memory materials: A review [J]. Materials and Design, 2012, 33: 577–640.
- [5] BIL C, MASSEY K, ABDULLAH E J. Wing morphing control with shape memory alloy actuators [J]. Journal of Intelligent Material Systems and Structures, 2013, 24: 879–898.
- [6] HUMBEECK J V. Non-medical applications of shape memory alloys [J]. Materials Science and Engineering A, 1999, 273–275: 134–148.
- [7] KOUSBROEK R. Metal and ceramic biomaterials. Volume II: Strength and surface [M]. CRC Press, 2018: 63–90.
- [8] VRSALOVIĆ L, IVANIĆ I, KOŽUH S, GUDIĆ S, KOSEC B, GOJIĆ M. Effect of heat treatment on corrosion properties of CuAlNi shape memory alloy [J]. Transactions of Nonferrous Metals Society of China, 2018, 28: 1149–1156.
- [9] SUN Y S, LORIMER G W, RIDLEY N. Microstructure and its development in Cu–Al–Ni alloys [J]. Metall Trans A, 1990, 21: 575–588.
- [10] SUGIMOTO K, KAMEI K, MATSUMOTO H, KOMATSU S, AKAMATSU K, SUGIMOTO T. Grain-refinement and the related phenomena in quaternary Cu–Al–Ni–Ti shape memory alloys [J]. Le Journal de Physique Colloques, 1982, 43: 761–766.
- [11] ASTM. Copper and copper alloys [S]. 2001.
- [12] European Copper Institute. Copper as electrical conductive material with above-standard performance properties [EB/OL]. <http://conductivity-app.org/single-article/cu-overview>. 2012.
- [13] FAULKNER M G, AMALRAJ J J, BHATTACHARYYA A. Experimental determination of thermal and electrical properties of Ni–Ti shape memory wires [J]. Smart Mater Struct, 2000, 9: 632–639.
- [14] GOMIDŽELOVIĆ L, POŽEGA E, KOSTOV A, VUKOVIĆ N, KRSTIĆ V, ZIVKOVIĆ D, BALANOVIĆ L. Thermodynamics and characterization of shape memory

- Cu–Al–Zn alloys [J]. Transactions of Nonferrous Metals Society of China, 2015, 25: 2630–2636.
- [15] MIYAZAKI S, OTSUKA K. The fracture of Cu–Al–Ni shape memory alloy [J] Transactions of the Japan Institute of Metals, 1981, 22: 244–252.
- [16] UĞUR S. Influences of 2.5wt% Mn addition on the microstructure and mechanical properties of Cu–Al–Ni shape memory alloys [J]. International Journal of Minerals, Metallurgy and Materials, 2010, 17: 192–198.
- [17] RECARTE V, PÉREZ-SÁEZ R B, SAN JUAN J, BOCANEGRA E H, NÓ M L. Influence of Al and Ni concentration on the martensitic transformation in Cu–Al–Ni shape-memory alloys [J]. Metallurgical and Materials Transactions A, 2002, 33: 2581–2591.
- [18] LEE J S, WAYMAN C M. Grain refinement of a Cu–Al–Ni shape memory by Ti and Zr additions [J]. Transactions of the Japan Institute of Metals, 1986, 27(8): 584–591.
- [19] SAUD S N, HAMZAH E, ABUBAKAR T, BAKHSHESHIRAD H R. Correlation of microstructural and corrosion characteristics of quaternary shape memory alloys Cu–Al–Ni–X (X=Mn or Ti) [J]. Transactions of Nonferrous Metals Society of China, 2015, 25: 1158–1170.
- [20] GUSTMANN T, DOS SANTOS J M, GARGARELLA P, KÜHN U, HUMBEECK J V, PAULY S. Properties of Cu-based shape-memory alloys prepared by selective laser melting [J]. Shape Memory and Superelasticity, 2017, 3: 24–36.
- [21] CAVA R D. Production and characterization of atomized powders with metastable structure of the Cu–51.9Zr–2.6Al–6.0Y amorphizable alloy and characterization of the mechanical properties of the shape memory alloy Cu–11.35Al–3.2Ni–3.0Mn–0.5Zr obtained by spray forming [D]. Federal University of São Carlos, 2015.
- [22] WOHLERS T, GORNET T. History of additive manufacturing [R]. Wohlers Report, 2016.
- [23] ZHAI Y, LADOS D A, LAGOY J L. Additive manufacturing: Making imagination the major limitation [J]. JOM, 2014, 66: 808–816.
- [24] COLOPI M, CAPRIO L, DEMIR A G, PREVITALI B. Selective laser melting of pure Cu with a 1 kW single mode fiber laser [J]. Procedia CIRP, 2018, 74: 59–63.
- [25] MAZZER E M, KIMINAMI C S, GARGARELLA P, CAVA R D, BASILIO L A, BOLFARINI C. Atomization and selective laser melting of a Cu–Al–Ni–Mn shape memory alloy [J]. Materials Science Forum, 2015, 802: 343–348.
- [26] GARGARELLA P, KIMINAMI C S, MAZZER E M, CAVA R D, BASILIO L A, BOLFARINI C. Phase formation, thermal stability and mechanical properties of a Cu–Al–Ni–Mn shape memory alloy prepared by selective laser melting [J]. Materials Research, 2015, 18: 35–38.
- [27] WANG X B, KUSTOV S, HUMBEECK J V. A short review on the microstructure, transformation behavior and functional properties of NiTi shape memory alloys fabricated by selective laser melting [J]. Materials, 2018, 11(9): 1683.
- [28] BAUMERS M, DICKENS P, TUCK C, HAGUE R. The cost of additive manufacturing: Machine productivity, economies of scale and technology-push [J]. Technological Forecasting and Social Change, 2016, 102: 193–201.
- [29] Desktop Metal Inc. Studio System™. Office-friendly metal 3D printing [EB/OL]. <https://www.desktopmetal.com/products/studio/>. 2020–01–16.
- [30] TANG S M, CHUNG C Y, LIU W G. Preparation of Cu–Al–Ni-based shape memory alloys by mechanical alloying and powder metallurgy method [J]. Journal of Materials Processing Technology, 1997, 63: 307–312.
- [31] GERA D. Processing of Cu–11.8Al–3.2Ni–3Mn–0.5Zr shape memory alloy through powder metallurgy [D]. Federal University of São Carlos, 2017.
- [32] DOS SANTOS J. Atomization and consolidation by selective laser fusion of Cu–11.8Al–3.2Ni–3.0Mn–0.5Zr alloy with shape memory effect [D]. Federal University of São Carlos, 2015.
- [33] CAVA R D, BOLFARINI C, KIMINAMI C S, MAZZER E M, BOTTA FILHO W J, GARGARELLA P. Spray forming of Cu–11.85Al–3.2Ni–3Mn (wt%) shape memory alloy [J]. Journal of Alloys and Compounds, 2015, 615: 602–606.
- [34] GERA D, SOYAMA J, CAVA R D, SPINELLI J E, KIMINAMI C S. The influence of sintering parameters in the microstructure and mechanical properties of a Cu–Al–Ni–Mn–Zr shape memory alloy [J]. Advanced Engineering Materials, 2018, 20: 1800372.
- [35] LIU P S, CHEN G F. Application of porous metals [J]. Porous Materials, 2014: 113–188.
- [36] BREZINA P. Heat treatment of complex aluminium bronzes [J]. International Metals Reviews, 1982, 27: 77–120.
- [37] HUMBEECK J V, van HULLE D, DELAEY L, ORTÍN J, SEGUÍ C, TORRA V A two-stage martensite transformation in a Cu–13.99 mass% Al–3.5 mass% Ni alloy [J]. Transactions of the Japan Institute of Metals, 1987, 28: 383–391.
- [38] KAYA M, ORHAN N, TOSUN G. Phase transformation behaviours of porous NiTi SMA fabricated as hollow and solid cylinders by SHS [J]. Materials Science and Technology, 2010, 26: 522–527.
- [39] BORMANN T, MÜLLER B, SCHINHAMMER M, KESSLER A, THALMANN P, DE WILD M. Microstructure of selective laser melted nickel–titanium [J]. Materials Characterization, 2014, 94: 189–202.
- [40] IMAI K, IKESHOJI T T, NAKAMURA K, NISHIDA M, SUGITANI Y, KYOGOKU H. Fabrication of Cu–Al–Ni shape memory alloy by selective laser melting process [J]. Materials Science Forum, 2018, 941: 1570–1573.

## 选区激光熔化和传统粉末冶金法制备 Cu–Al–Ni–Mn–Zr 形状记忆合金的对比

Dennis GERA<sup>1,2</sup>, Jonadabe SANTOS<sup>1,2</sup>, Cláudio S. KIMINAMI<sup>1,2</sup>, Piter GARGARELLA<sup>1,2</sup>

1. Postgraduate Program in Materials Science and Engineering, Federal University of São Carlos, São Carlos, Brazil;

2. Materials Engineering Department, Federal University of São Carlos,

R. Washington Luís, km 235-SP 310, São Carlos, Brazil

**摘要:** 研究和分析选区激光熔化(SLM)与传统粉末冶金(PM)法制备 Cu–11.3Al–3.2Ni–3.0Mn–0.5Zr 形状记忆合金的显微组织特征和热稳定性差异。PM 样品是将 106~180  $\mu\text{m}$  预合金粉末在氩气气氛、1060  $^{\circ}\text{C}$  下烧结制备的,无辅助加工,SLM 样品是在 Cu–10Sn 基板上熔化 32~106  $\mu\text{m}$  的预合金粉末制备的。通过维氏硬度试验评价材料的力学性能,采用差示扫描量热法测定马氏体相变温度,采用 X 射线衍射谱鉴定相成分,利用光学显微镜和扫描电子显微镜分析显微组织特征。结果表明,两种方法制备的合金中均发现  $\beta'_1$  马氏体相,而在 PM 样品中存在粗大的马氏体变体。传统的粉末冶金样品在室温下会形成晶间共析成分和稳定的奥氏体。PM 样品具有与 SLM 样品相似的平均硬度值,而与孔隙率相关的标准偏差较高。SLM 样品具有可逆的马氏体相变( $T_0=171\text{ }^{\circ}\text{C}$ ),而 PM 样品没有形状记忆效应。

**关键词:** 形状记忆合金; 粉末冶金; 增材制造; 选区激光熔化; Cu 基合金

(Edited by Bing YANG)